Supporting information

Copper single atom-modulated functionalization of iron clusters on porous carbon nanosheet for oxygen reduction reaction

Lingmin Wu[a], Yinghua Wang[a], Chunfeng Shao[b], Liming Wang[a], Baitao Li[a,*]

[a] Guangdong Provincial Key Laboratory of Fuel Cell Technology, School of Chemistry and Chemical Engineering, South China University of Technology, Guangzhou 510640, China

[b] Anhui Province Key Laboratory of Pollutant Sensitive Materials and Environmental Remediation, Department of Materials Science and Engineering, Huaibei Normal University, Huaibei 235000, China

*E-mail: btli@scut.edu.cn (Baitao Li)

1. Experiment

Synthesis of FeCu-NC-*x* catalyst. The synthesis was carried out by the solid phase reaction. First, 48 mg of $Fe(NO_3)_3 \cdot 9H_2O$, 27.6 mg of $Cu(NO_3)_2 \cdot 3H_2O$, 0.25 g of 1,10-phenanthroline and definite molar ratio of melamine and urea were ball-milled for 30 min (Table S1). Then, the solid mixture was pyrolyzed in a tube furnace at 900 °C for 2 h under N_2 atmosphere. The obtained solid was subsequently leached in 2 mol L^{-1} HNO_3 for 12 h to remove any metal particles, and then pyrolyzed again at 900 °C for 2 h. The catalyst was labeled as FeCu-NC-*x*, where *x* was the molar ratio of melamine and urea (*x* = 0.5, 1, 2). As a comparison, FeCu-NC-M and FeCu-NC-U were synthesized in a similar process, but only with the addition of the melamine (M) or urea (U), respectively.

Synthesis of Fe-NC-0.5 and Cu-NC-0.5 catalyst. Similarly, Fe-NC-0.5 and Cu-NC-0.5 catalysts were synthesized according to the same method as FeCu-NC-0.5. The dosage of metal

salt was 48 mg of $Fe(NO_3)_3 \cdot 9H_2O$ and 28.7 mg of $Cu(NO_3)_2 \cdot 3H_2O$, respectively.

2. Characterization

The morphology of catalyst was observed using a SU8220 field emission scanning electron microscope (SEM, Hitachi) and a JEM-2100F transmission electron microscopy (TEM, JEOL). The elemental distribution of Fe, Cu, N, C and O atoms were studied using a XFlash 6T-60 energy dispersive X-ray spectrometer (EDX, Bruker) attached to TEM. Atomic level resolution was detected and distinguished using a Themis Z aberration-corrected high-angle annular dark-field scanning transmission electron microscope (HAADF-STEM, FEI) and Electron Energy Loss Spectroscopy (EELS, Gatan 965). The local structural information around Fe and Cu atoms were investigated in detail using X-ray absorption spectroscopy (XAS) on a BL20U station of Shanghai Synchrotron Radiation Facilities at fluorescence excitation mode, which was operated at 3.5 GeV with a maximum current of 220 mA. Crystal structure was determined using a D8 Advance X-ray powder diffractometer (XRD, Bruker) with the scattering angle of 2θ from 5° to 90°. Elemental compositions (Fe and Cu) in the bulk phase were analyzed via an Optima 8300 inductively coupled plasma optical emission spectroscopy (ICP-OES, PerkinElmer), while nitrogen was analyzed via a Vario EL cube elemental analyzer (Elementar). Valence state, elemental composition on the catalyst surface were studied using an ESCALAB 250Xi X-ray photoelectron spectroscopy (XPS, Thermo Fisher Scientific) and Auger electron spectroscopy (XAES) spectra. The C 1*s* line at 284.8 eV was utilized for calibrating the binding energy in the spectra. The pore characteristics and surface area were analyzed by a nitrogen adsorption–desorption on an ASAP 2460 physisorption instrument (Micromeritics). The specific surface area was calculated with Brunauer-Emmett-Teller method and pore size distribution was plotted using density functional theory. Prior to test, the catalyst was pretreated at 100 °C for 6 h under vacuum to remove any adsorbed species.

3. Electrochemical measurement

The oxygen reduction reaction (ORR) performance was analyzed using an IGS-6030 electrochemical workstation (Guangzhou Ingsens Sensor Technology Co., Ltd., China) equipped with a three-electrode system. A 5 mm-diameter glassy carbon rotating disk electrode

(RDE) was used as the working electrode, while a saturated calomel electrode (SCE) and a carbon rod was employed as the reference and counter electrodes, respectively. The catalyst ink coated onto the working electrode was prepared dispersing 4 mg of catalyst in 1.0 mL of a 0.25% Nafion solution with ethanol as the solvent. The catalyst loading for the synthesized catalyst was 0.408 mg cm^{-2}, whereas 0.204 mg cm^{-2} for 20 wt% Pt/C catalyst. Linear sweep voltammetry (LSV) test was conducted in O_2-saturated electrolytes at various rotation speeds (625, 900, 1225, 1600, 2025 rpm) with a scan rate of 10 mV s^{-1}. The potential sweep window was selected from 0.2 to -0.8 V vs. SCE in 0.1 M KOH solution, and from 0.4 to -0.6 V vs. SCE in 0.05 M phosphate buffer solution (PBS) solution. All the potentials appeared in the figures and tables were calibrated to the reversible hydrogen electrode (RHE).

The ORR reaction kinetics was studied using Koutechy-Levich (K-L) equation (1) and (2):

$$\frac{1}{J} = \frac{1}{J_L} + \frac{1}{J_K} = \frac{1}{B\omega^{\frac{1}{2}}} + \frac{1}{J_K} \quad (1)$$

$$B = 0.2nFC_0D_0^{\frac{2}{3}}v^{-\frac{1}{6}} \quad (2)$$

Where J, J_L, J_K is the overall measured current density, diffusion-limiting current density and kinetic current density, respectively, and ω is the electrode rotation speed (rpm), n is the number of electrons transferred in ORR reaction, F is Faraday constant (96485 C mol^{-1}), C_0 is the saturated O_2 concentration (1.26×10^{-6} mol cm^{-3}), D_0 is the diffusion coefficient of O_2 (2.7×10^{-5} cm^2 s^{-1}), v is the kinematic viscosity of electrolyte (0.01 cm^2 s^{-1}).

The determination of the electron transfer number (n) was also performed using a rotating ring-disk electrode (RRDE) at rotation rate of 1600 rpm when the ring electrode voltage was kept at 1.5 V vs. RHE. The n and peroxide yield (HO_2^- %) were obtained from disk (i_d) and ring (i_r) current according to equations (3) and (4):

$$n = \frac{4 \mid i_d \mid}{\mid i_d \mid + \frac{i_r}{N}} \quad (3)$$

$$HO_2^-\% = \frac{\frac{2i_r}{N}}{\mid i_d \mid + \frac{i_r}{N}} \times 100\% \quad (4)$$

Where N is the collection efficiency of Pt ring (N=37%).

The stability of catalyst was measured using current-time (*i-t*) chronoamperometric method at half-wave potential ($E_{1/2}$). The durability of the catalyst was evaluated using accelerated durability test (ADT) with the scan rate of 0.2 mV s^{-1} from -0.8 to 0 V vs. SCE.

4. Computational method

Density functional theory (DFT) calculation was conducted through the Vienna Ab initio Simulation Package (VASP) with the projector augment wave method. Generalized gradient approximation of the Perdew-Burke-Ernzerhof (PBE) functional was used as the exchange-correlation functional. The Brillouin zone was sampled using the 2x2x1 Monkhorst-Pack *k*-point mesh for surface calculation. A cutoff energy of 400 eV, energy of 1×10^{-5} eV and force of 0.02 eV $Å^{-1}$ was set for the structure relaxation until the convergence. A vacuum layer of 15 Å was constructed to eliminate interactions between periodic structures.

The free energy of each elementary step involving proton/electron transfer during oxygen reduction reaction (ORR) was carried out with computational hydrogen electrode method, and it was computed based on the equation (5):

$$\Delta G = \Delta E_{DFT} + \Delta E_{ZPE} - T\Delta S - eU \quad (5)$$

Where ΔE_{DFT}, ΔE_{ZPE} and ΔS are electronic energy, zero-point energy, and entropy difference between absorbed intermediate system and catalyst, respectively, T is the temperature (25°C), e is the transferred electron number and U is the applied potential vs RHE.

The adsorption energies E_{ads*O2} was calculated according to equation (6):

$$E_{ads*O2} = E_{system} - E_{catalyst} - E_{O2} \quad (6)$$

Where E_{system} represent the total energy of the oxygen adsorbed system.

5. Construction of Zn-Air battery and related calculations

The button-typed Zn-air battery was assembled with 0.2 g of zinc powder (99.99%) as the anode and the mixed solution of 6 M KOH and 2 M $Zn(CH_3COO)_2$ as the electrolyte. The cathode consisted of three components: the catalyst, Ni-foam (as a current collector) and carbon paper (as a gas diffusion layer). The catalyst ink was prepared by dispersing 5 mg of catalyst in a mixture of 40 μL of Nafion, 0.5 mL of ethanol and 0.5 mL of deionized water. Then the ink was drop-cast onto the Ni-foam and carbon paper to achieve a loading of 4 mg cm^{-2} (2 mg cm^{-2} for Pt/C). The discharge energy density curves and capacity curves were conducted with 10

mg of zinc powder at a current density of 10 mA cm^{-2}, and the discharge/charge curves and stability test was both measured at 10 mA cm^{-2}. All data were collected using a CHI660D electrochemical workstation at ambient temperature.

The calculation of relevant specific capacity (mAh gZn^{-1}) and energy density (Wh $kgZn^{-1}$) could refer to our previous work [1].

6. Assembly of Microbial fuel cell (MFC) and related calculations

The single-chamber microbial fuel cell (MFC) with a volume of 28 mL was constructed with the pre-colonized anode, which had electroactive microbes growing on after 4-week colonization in anaerobic domestic effluent. The cathode was carbon cloth loaded with catalyst. The pretreatment for both the cathodic and anodic carbon cloth was carried out following the procedure outlined in our previous work [2]. The catalyst ink was prepared by mixing every 1 mg of catalyst in a solution consisting of 0.83 μL of deionized water, 6.67 μL of Nafion, and 3.33 μL of isopropanol. The loading amount of the prepared catalyst was set to 4 mg cm^{-2}, while this for Pt/C was maintained at 2.5 mg cm^{-2}, which was in alignment with the common practice in MFC research [3]. Additionally, the electrolyte in MFC was composed of 7 mL of effluent from a municipal sewage treatment plant (Guangzhou) and 21 mL of neutral culture medium. The culture medium was prepared in advance with 8.4 g L^{-1} of CH_3COONa, 105 mL L^{-1} of mineral solution, and 42 mL L^{-1} of nutrient solution. A fixed external resistor of 1000 Ω was employed to connect the cathode and anode. The voltage was continuously monitored every 15 min using a self-programmed data acquisition system.

The power density measurement and polarization curve were acquired by applying different external resistance in the range of 33000 to 82 Ω. The voltage under each applied external resistance was measured using a UT33C digital multimeter (Uni-Trend Technology Co., Ltd. China). The current corresponding to the output voltage was calculated according to Ohm's law.

The chemical oxygen demand (COD) removal and coulombic efficiency (CE) were analyzed using a COD-571 detector (Shanghai Precision and Scientific Instrument Co., China), as reported in our previous work [1].

Electrochemical impedance spectroscopy (EIS) was tested using an electrochemical

workstation (CHI 660D, Shanghai Chenhua Instrument Co., Ltd). The assembled cathode, anode and MFC solution was used as the working electrode, counter electrode and electrolyte, respectively. A saturated Ag/AgCl (3 mol L^{-1} of KCl) electrode was used as a reference electrode. Impedance spectra were collected in the frequency range from 10^5 to 10^{-2} Hz with sinusoidal amplitude of 10 mV.

FIGURES AND TABLES

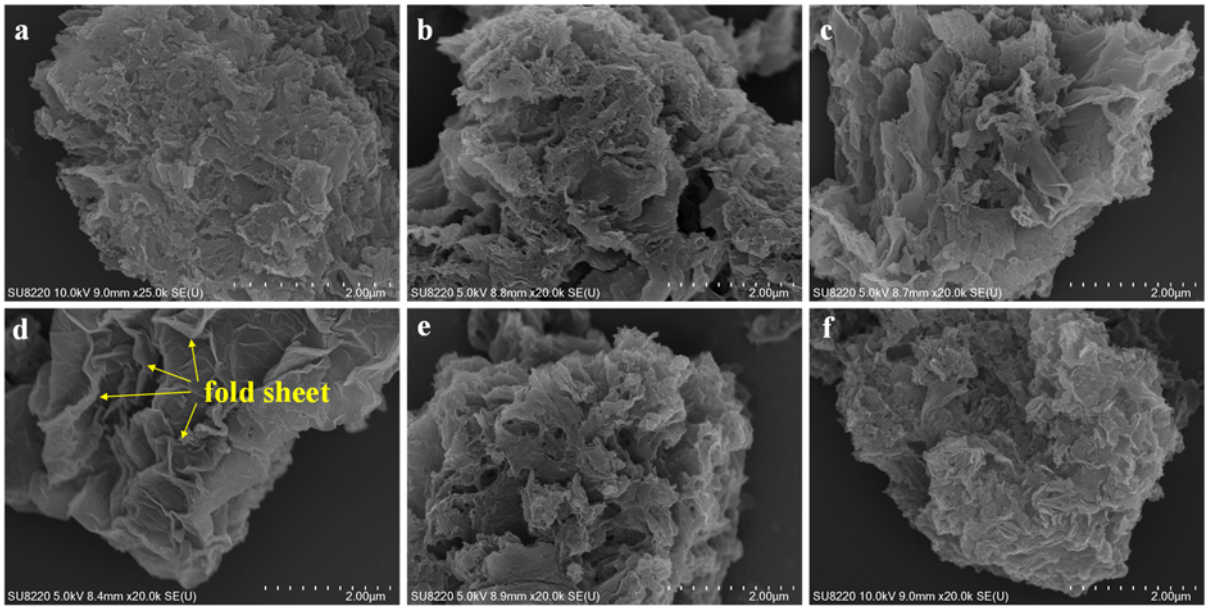

Figure S1. SEM images of FeCu-NC-1 (a), FeCu-NC-2 (b), FeCu-NC-M (c), FeCu-NC-U (d), Fe-NC-0.5 (e) and Cu-NC-0.5 (f).

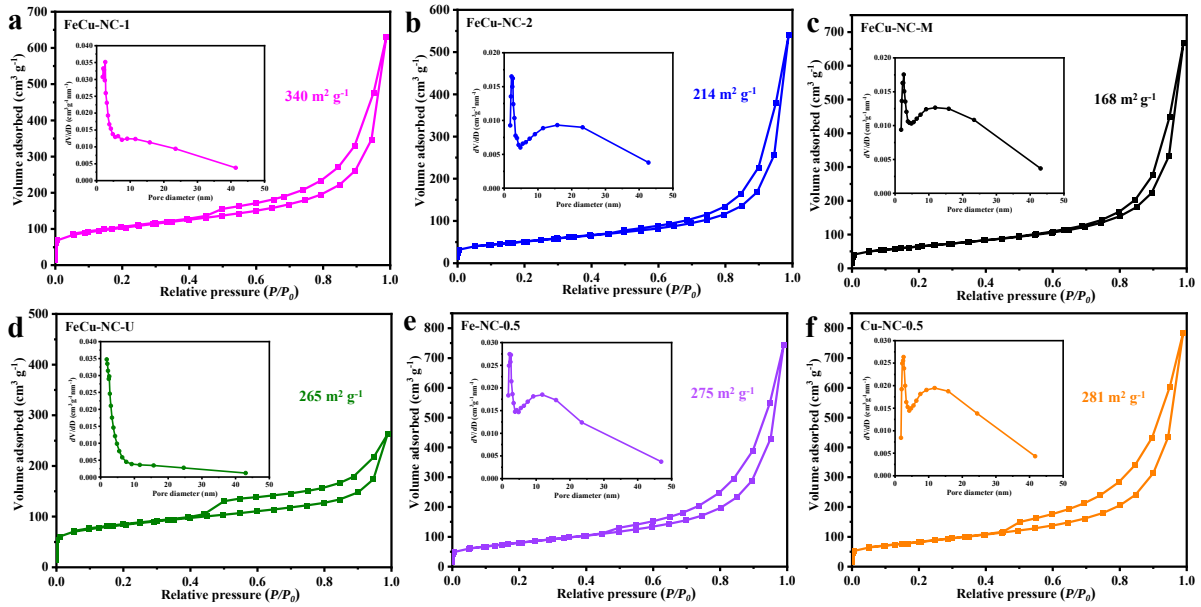

Figure S2. Nitrogen sorption isotherms and the corresponding pore size distribution of FeCu-NC-1 (a), FeCu-NC-2 (b), FeCu-NC-M (c), FeCu-NC-U (d), Fe-NC-0.5 (e) and Cu-NC-0.5(f).

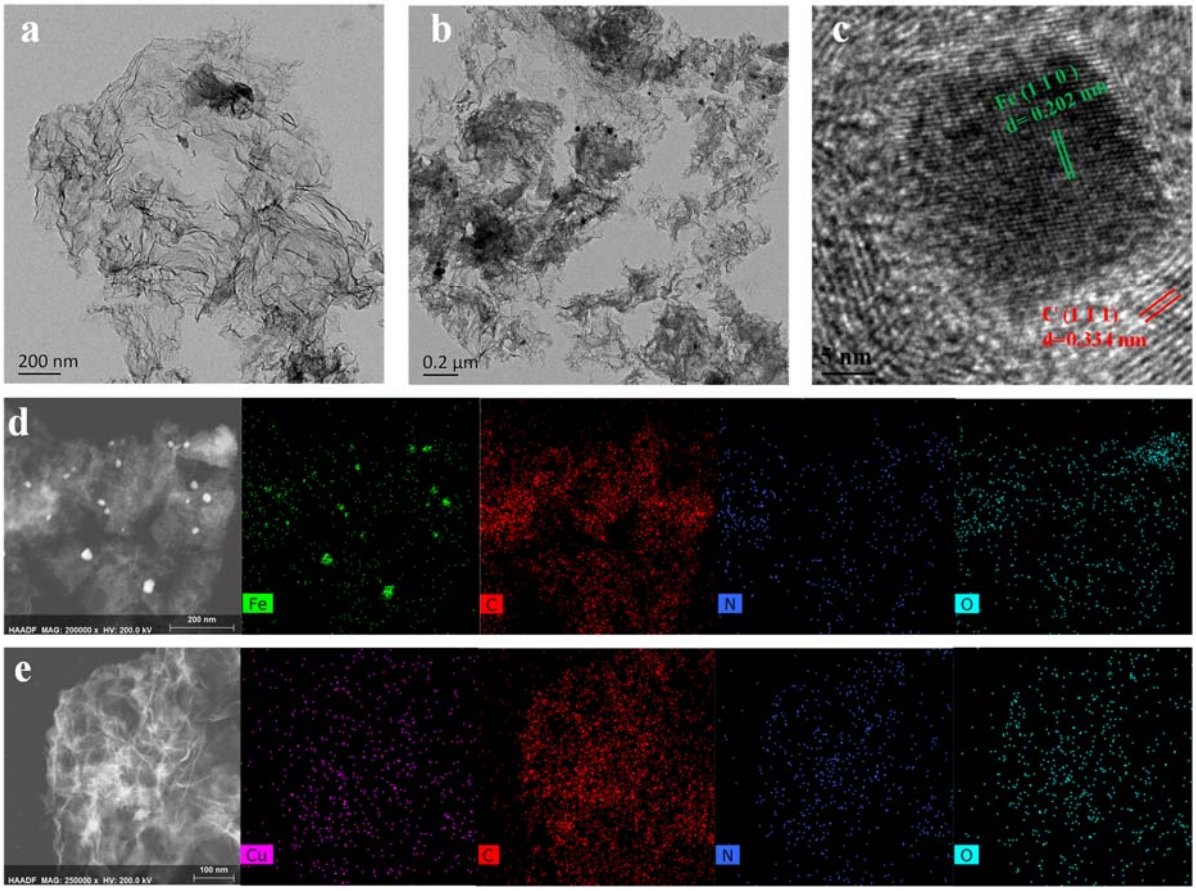

Figure S3. TEM images of Cu-NC-0.5 (a) and Fe-NC-0.5 (b, c), and HAADF-STEM image and corresponding elements distribution of Fe-NC-0.5 (d) and Cu-NC-0.5 (e).

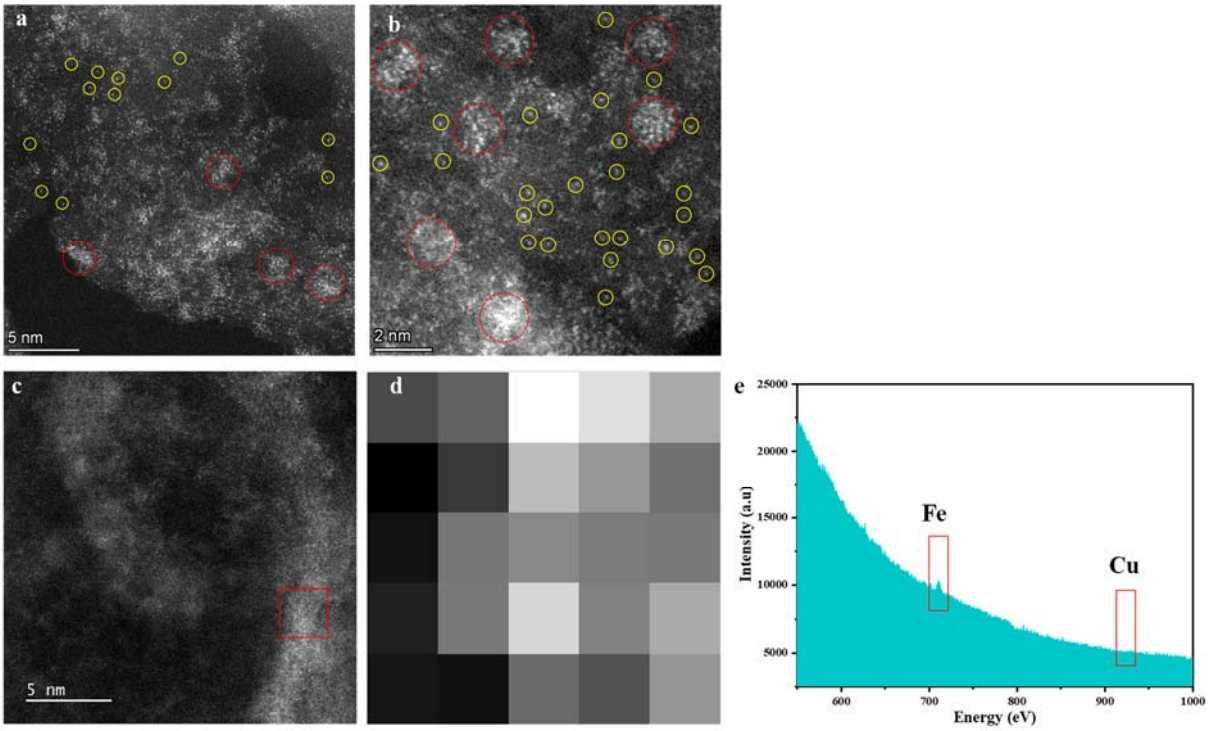

Figure S4. Aberration-corrected HAADF-STEM image (a, b, clusters marked by red circles and single atoms marked by yellow circles), EELS test model with high-loss (d) corresponding to the red area in (c) and the EELS spectrum (e) of FeCu-NC-0.5 catalyst.

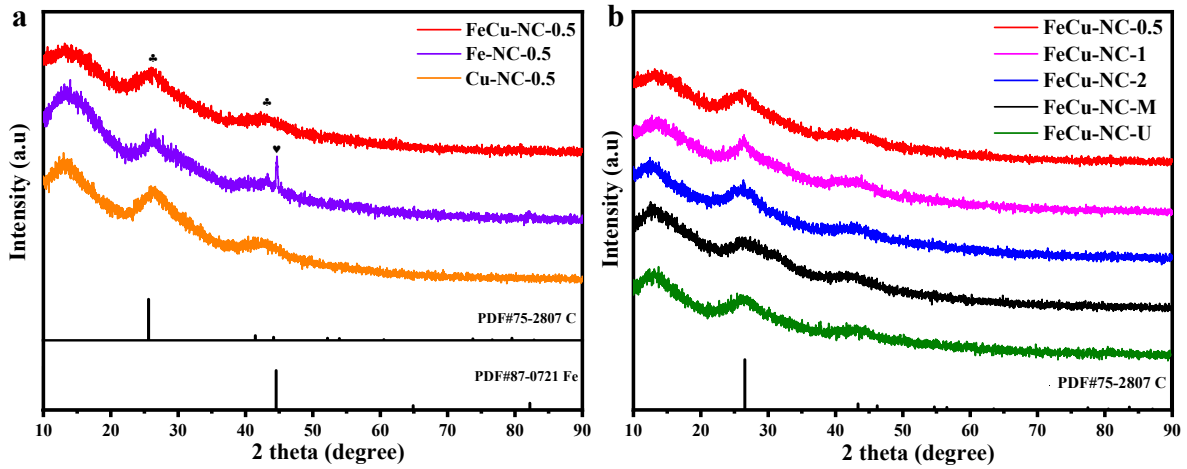

Figure S5. XRD patterns of FeCu-NC-0.5, Fe-NC-0.5 and Cu-NC-0.5 (a), and FeCu-NC-*x*, FeCu-NC-M and FeCu-NC-U catalysts (b).

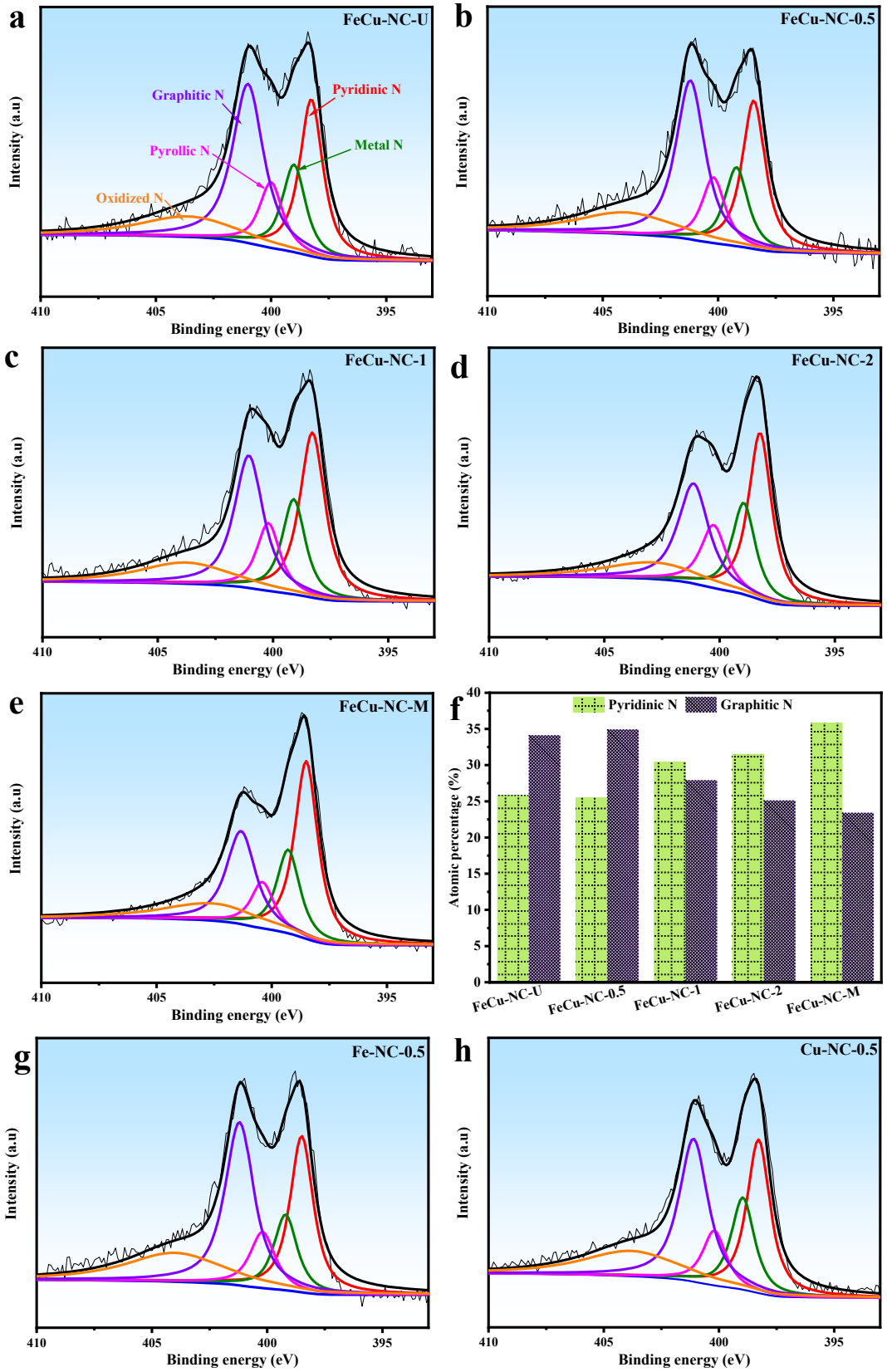

Figure S6. N 1*s* XPS profile of FeCu-NC-U (a), FeCu-NC-0.5 (b), FeCu-NC-1 (c), FeCu-NC-2 (d), FeCu-NC-M (e), Fe-NC-0.5 (g), Fe-NC-0.5 (h) and the N content of synthesized dual metallic catalysts (f).

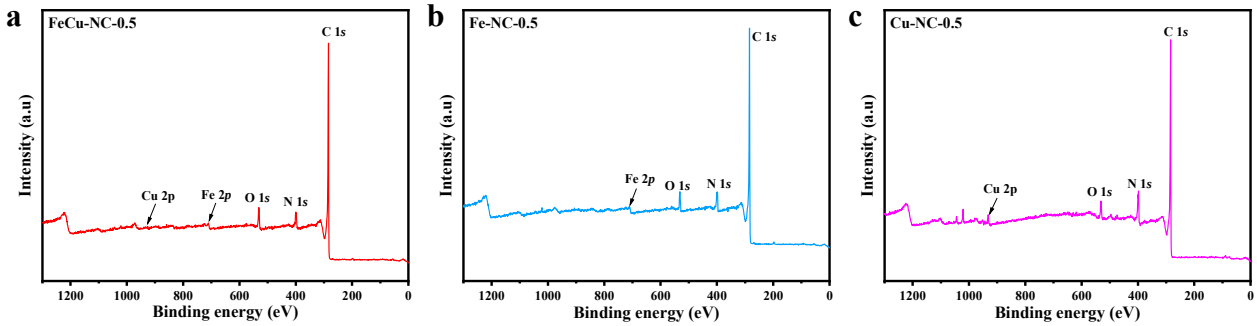

Figure S7. XPS survey patterns of FeCu-NC-0.5 (a), Fe-NC-0.5 (b) and Cu-NC-0.5 (c).

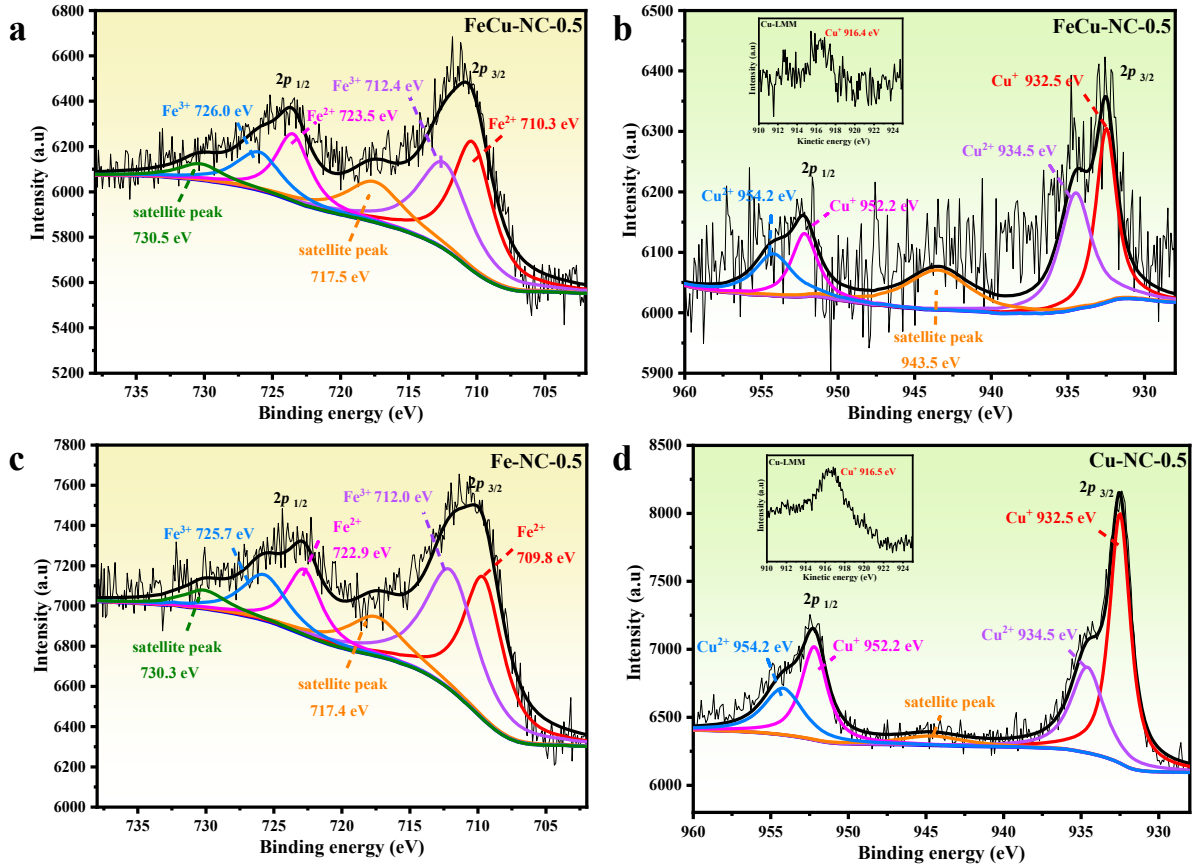

Figure S8. Fe 2*p* XPS profile of FeCu-NC-0.5 (a) and Fe-NC-0.5 (c); Cu 2*p* XPS profile and Cu-L3M45M45 Auger spectra (inset) of FeCu-NC-0.5 (b) and Cu-NC-0.5 (d).

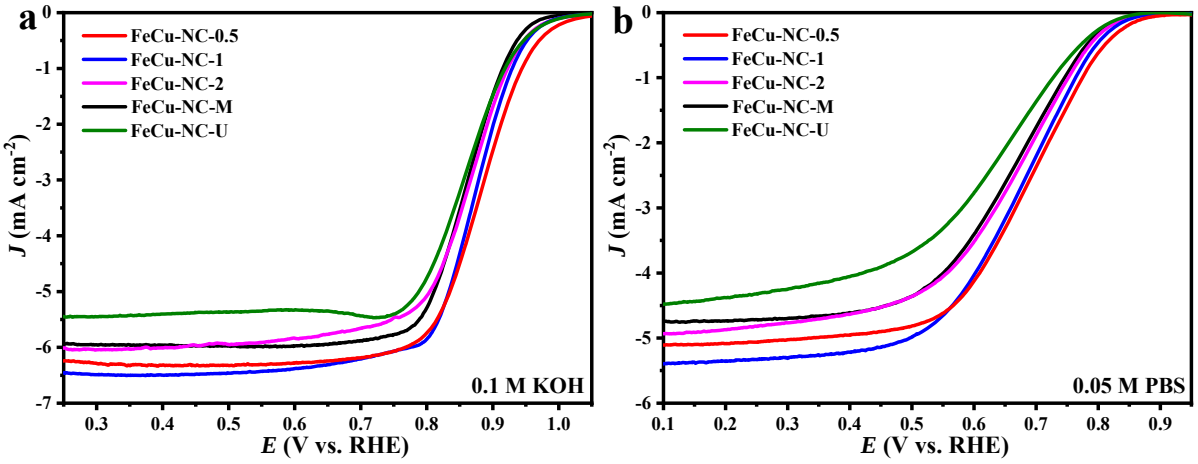

Figure S9. LSV curves tested at 1600 rpm of FeCu-NC-0.5, FeCu-NC-2, FeCu-NC-1, FeCu-NC-M, and FeCu-NC-U catalysts in 0.1 M KOH (a) and 0.05 M PBS solution (b).

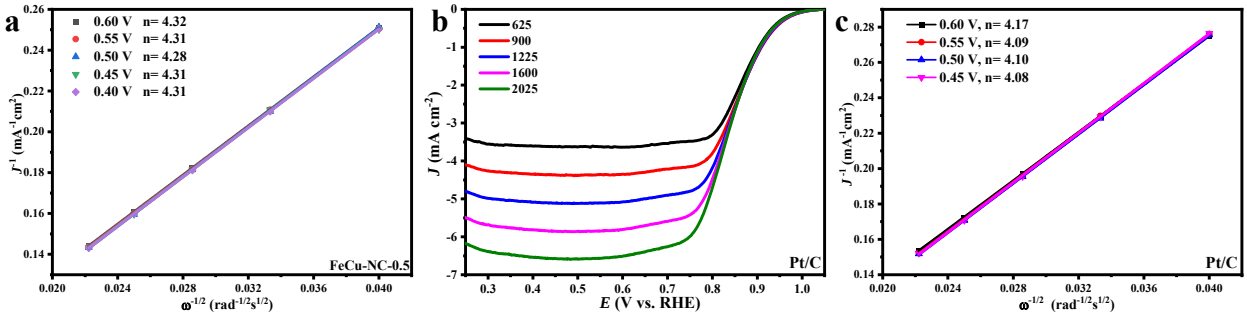

Figure S10. Corresponding electron transfer numbers (*n*) of FeCu-NC-0.5 (a) derived from the Koutecky-Levich (K-L) equation. LSV curves of Pt/C at different rotate speed from 625 to 2025 rpm in 0.1 M KOH (b) and the corresponding electron transfer numbers (*n*) of Pt/C (c).

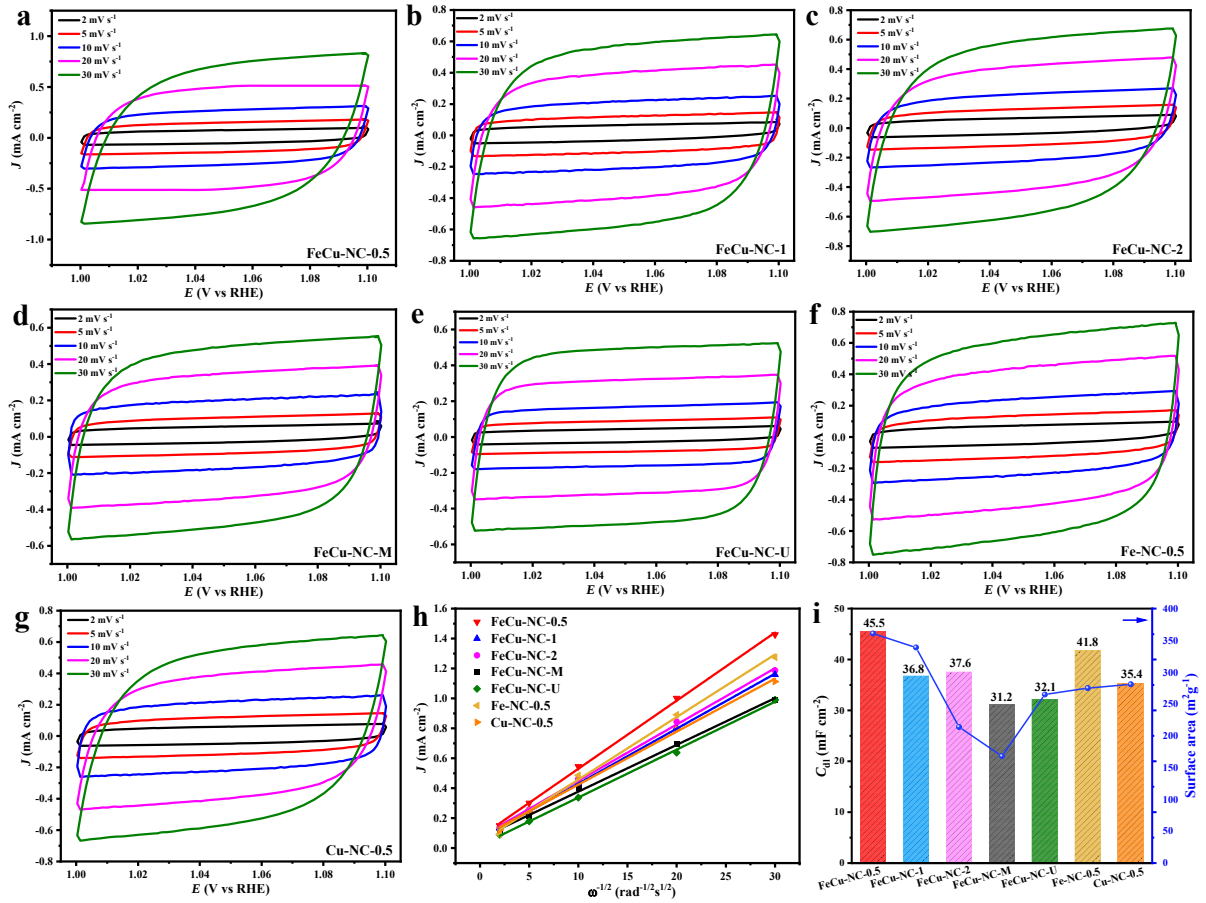

Figure S11. CV curves of FeCu-NC-0.5 (a), FeCu-NC-1 (b), FeCu-NC-2 (c), FeCu-NC-M (d), FeCu-NC-U (e), Fe-NC-0.5 (f) and Cu-NC-0.5 (g) at scan rates of 2, 5, 10, 20, 30 mV s^{-1} in N_2-saturated 0.1 M KOH, the plots of current densities at 1.05 V vs RHE as a function of scan rates (h) and the relationship between C_{dl} value and surface area (i).

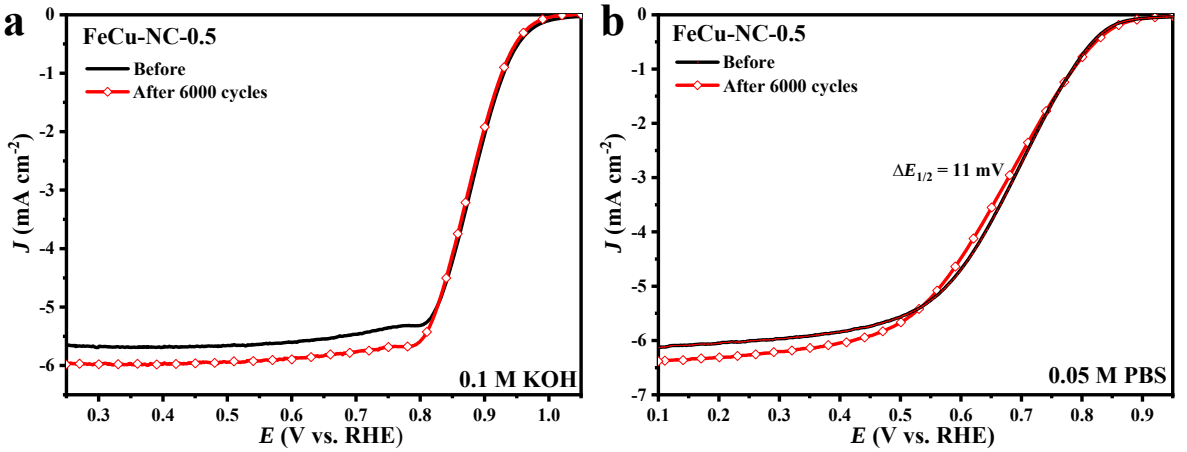

Figure S12. LSV curves of FeCu-NC-0.5 after ADT of 6000 cycles in O_2-saturated 0.1 M KOH (a) and 0.05 M PBS (b).

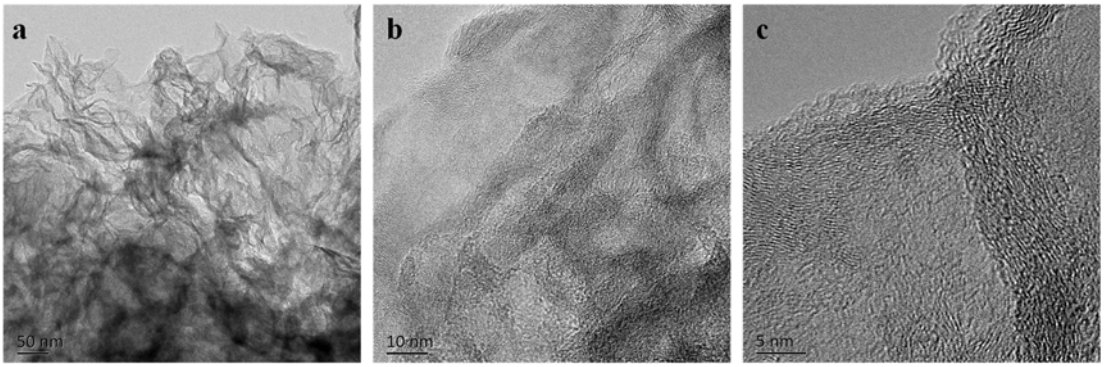

Figure S13. TEM images with different magnifications of FeCu-NC-0.5 after ADT test in O_2-saturated 0.1 M KOH.

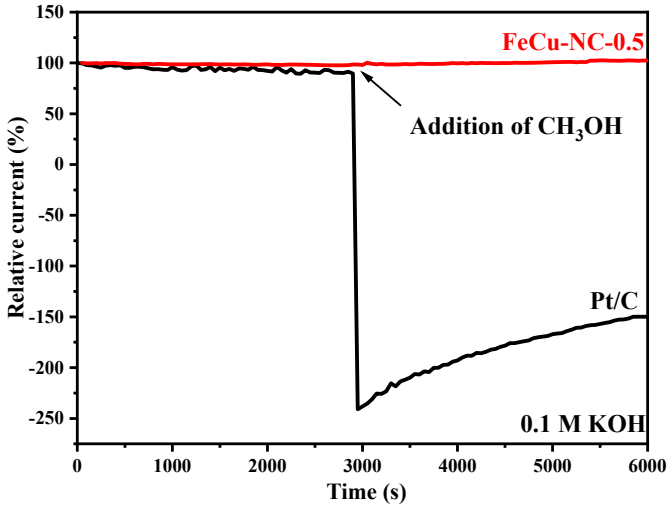

Figure S14. Methanol crossover effect of FeCu-NC-0.5 and Pt/C in O_2-saturated 0.1 M KOH.

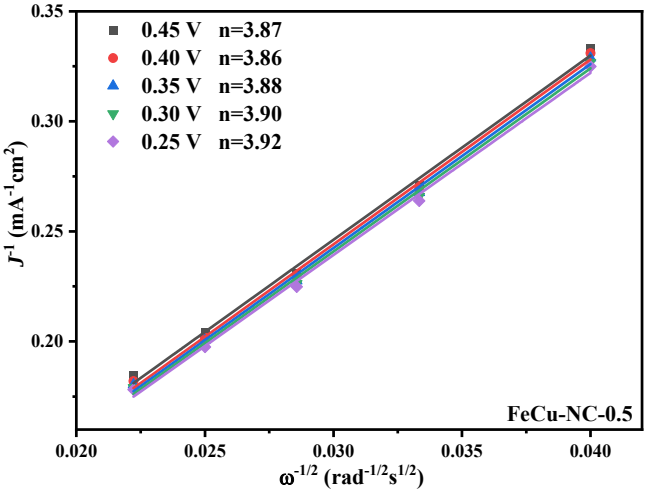

Figure S15. Electron transfer numbers of FeCu-NC-0.5 in 0.05 M PBS from the K-L equation.

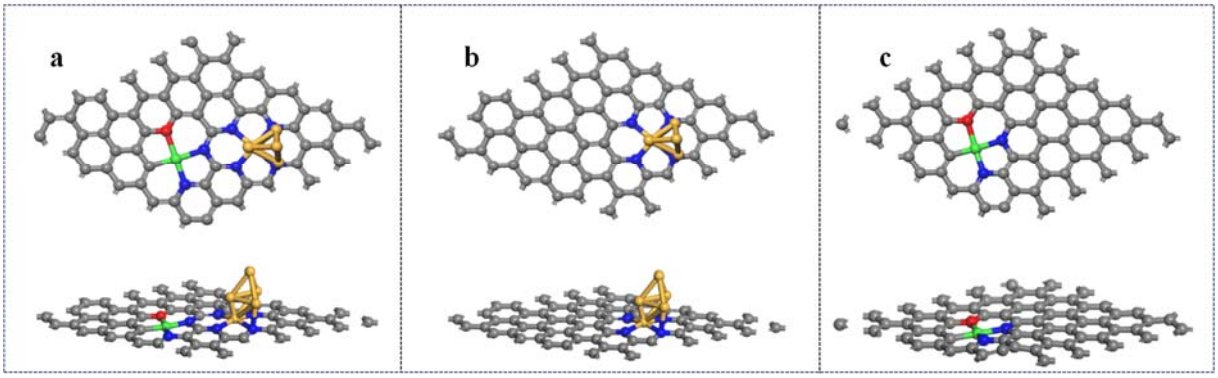

Figure S16. Top view (first panel) and side view (second panel) of the constructed Fe_5-CuN_2O (FeCu-NC-0.5) (a) and corresponding counterpart Fe_5 (b) and Cu-N_2O (c) models. Color interpretation: green (Cu atom), yellow (Fe atom), dark blue (N atom), red (O atom), and grey (C atom).

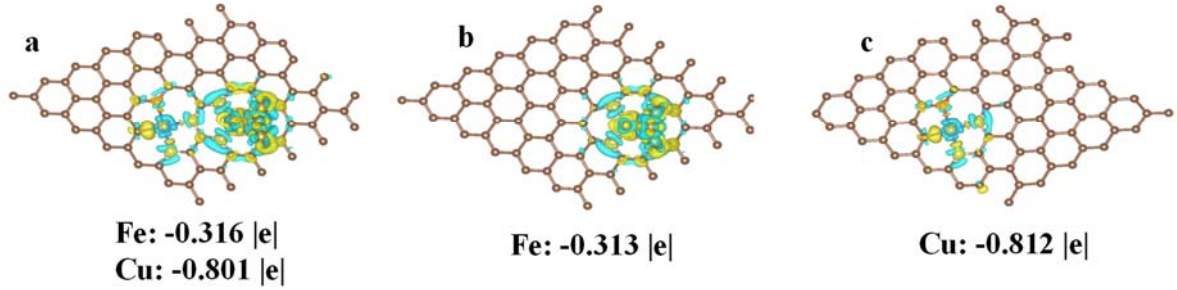

Figure S17. Differential charge density of Fe_5-CuN_2O (a), Fe_5 (b) and Cu-N_2O (c) models. Charge depletion and accumulation are respectively colored in blue and yellow.

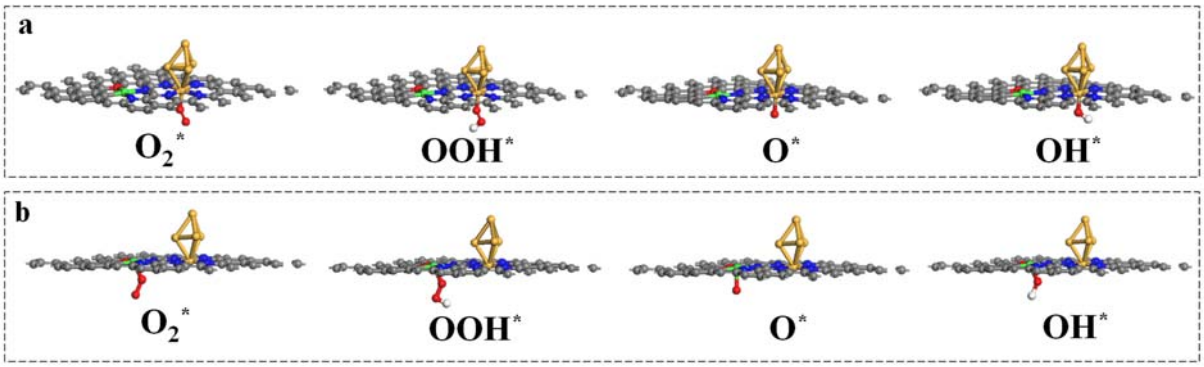

Figure S18. Geometric structures of intermediates adsorbed on Fe (a) and Cu (b) sites in Fe_5-CuN_2O model. Color interpretation: green (Cu atom), yellow (Fe atom), dark blue (N atom), red (O atom), white (H atom), and grey (C atom).

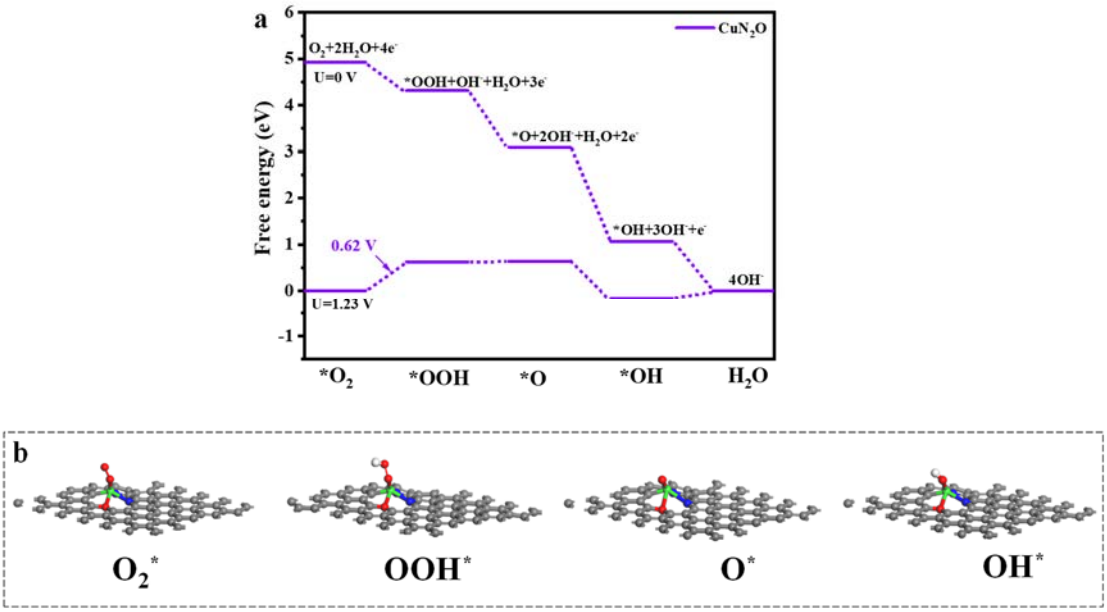

Figure S19. Free energy diagram in Cu-N_2O model (a) and geometric structures of intermediates adsorbed on Cu-N_2O model (b). Color interpretation: green (Cu atom), dark blue (N atom), red (O atom), white (H atom), and grey (C atom).

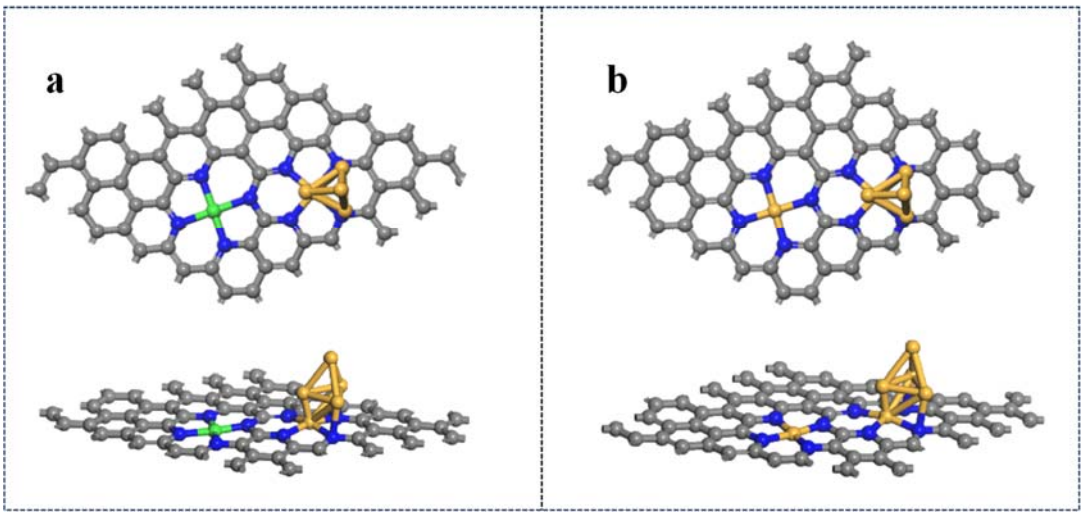

Figure S20. Top view (first panel) and side view (second panel) of the constructed Fe_5-CuN_4 (a) and Fe_5-FeN_4 (b) models. Color interpretation: green (Cu atom), yellow (Fe atom), dark blue (N atom) and grey (C atom).

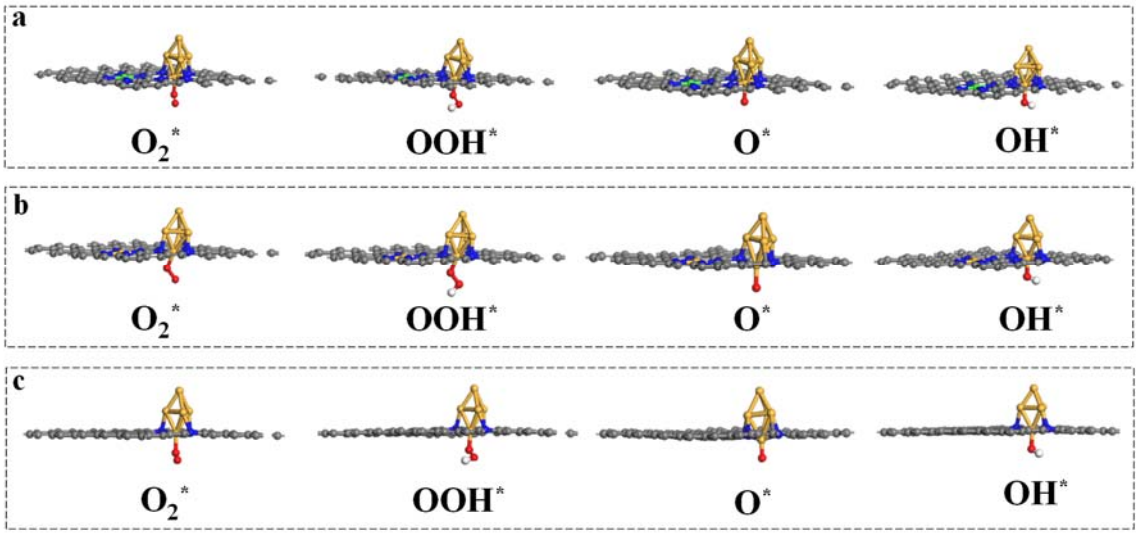

Figure S21. Geometric structures of intermediates adsorbed on Fe_5-CuN_4 (a), Fe_5-FeN_4 (b) and Fe_5 (c) models. Color interpretation: green (Cu atom), yellow (Fe atom), dark blue (N atom), red (O atom), white (H atom), and grey (C atom).

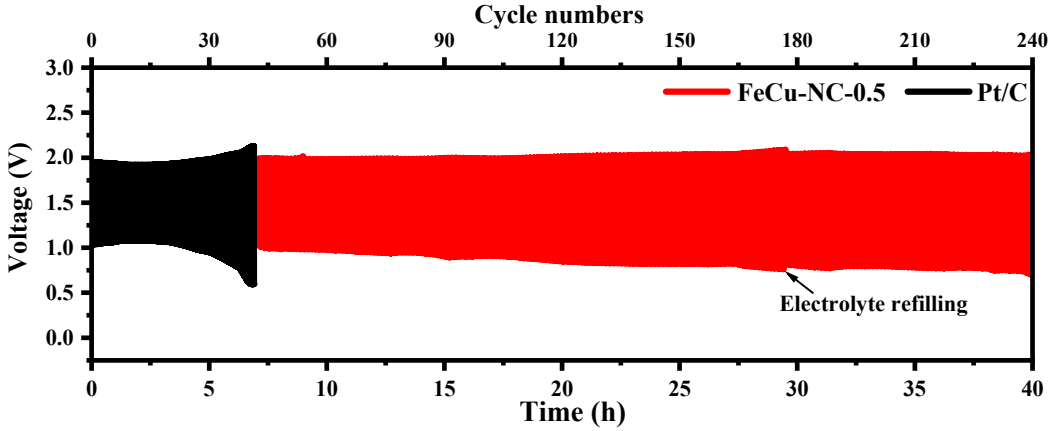

Figure S22. Discharge-charge curves of FeCu-NC-0.5 and Pt/C at 10 mA cm^{-2}.

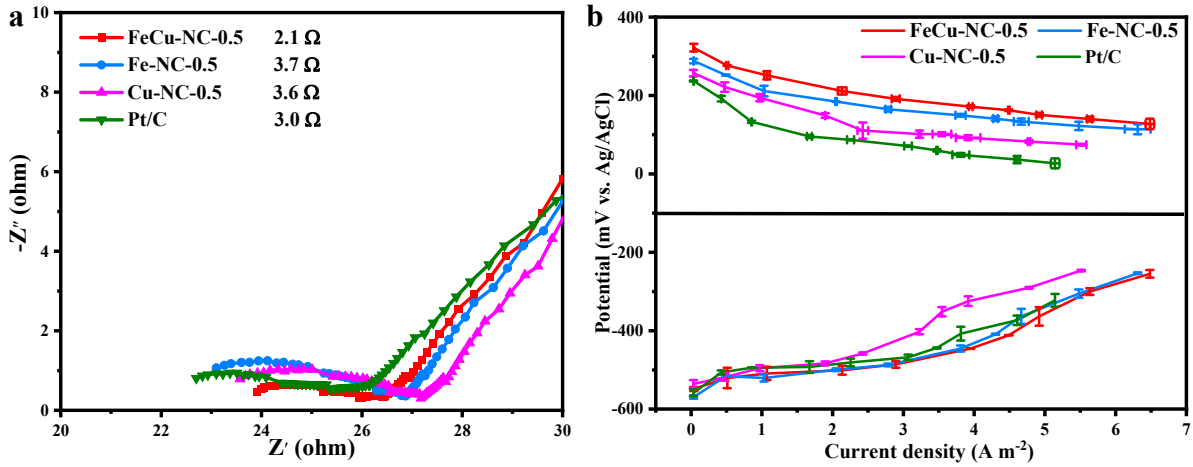

Figure S23. Cathodic resistance (a) and electrode potential (b) of MFCs with FeCu-NC-0.5, Fe-NC-0.5, Cu-NC-0.5 and Pt/C as catalysts.

Table S1. Dosage of raw materials in catalyst preparation

Catalyst	$Fe(NO_3)_3 \cdot 9H_2O$ (mg)	$Cu(NO_3)_2 \cdot 3H_2O$ (mg)	Melamine (mmol)	Urea (mmol)
FeCu-NC-0.5	48	28.7	7.0	14.0
FeCu-NC-1	48	28.7	10.5	10.5
FeCu-NC-2	48	28.7	14.0	7.0
FeCu-NC-M	48	28.7	21.0	0
FeCu-NC-U	48	28.7	0	21.0
Fe-NC-0.5	48	0	7.0	14.0
Cu-NC-0.5	0	28.7	7.0	14.0

Table S2. Textural parameters of all as-synthesized materials according to N_2 sorption isotherms.

Catalyst	Surface area ($m^2\ g^{-1}$)	Micropore area ($m^2\ g^{-1}$)	External area ($m^2\ g^{-1}$)	Pore volume ($cm^3\ g^{-1}$)	Average pore size (nm)
FeCu-NC-0.5	361	93	268	0.62	6.8
FeCu-NC-1	340	67	272	0.59	6.9
FeCu-NC-2	214	11	203	0.54	10.2
FeCu-NC-M	168	12	156	0.43	10.3
FeCu-NC-U	265	86	179	0.27	4.1
Fe-NC-0.5	275	10	265	0.65	9.4
Cu-NC-0.5	281	1	280	0.73	10.4

Table S3. Elemental contents (wt%) of nitrogen in the catalysts according to Elemental analysis.

Catalyst	N
FeCu-NC-0.5	9.34
FeCu-NC-1	12.81
FeCu-NC-2	14.35
FeCu-NC-M	10.35
FeCu-NC-U	6.41
Fe-NC-0.5	12.44
Cu-NC-0.5	11.84

Table S4. Elemental contents (atom%) and relative percentage of nitrogen species (%) according to XPS results.

Catalyst	Elemental contents (atom%)					Relative percentage of nitrogen species (%)				
	Fe	Cu	C	N	O	Pyridinic N	Metal-N	Pyrrolic N	Graphitic N	Oxidized N
FeCu-NC-0.5	0.94	0.18	86.5	7.25	5.14	25.5	13.6	11.3	34.9	14.7
FeCu-NC-1	1.16	0.22	82.6	8.40	7.62	30.4	16.0	11.4	27.9	14.2
FeCu-NC-2	1.01	0.23	82.4	9.70	6.66	31.5	17.2	13.1	25.1	13.0
FeCu-NC-M	0.91	0.19	82.0	10.6	6.30	35.8	16.9	9.3	23.4	14.5
FeCu-NC-U	0.96	0.19	84.1	7.26	6.96	25.8	14.4	10.8	34.1	14.9
Fe-NC-0.5	1.05	/	85.8	8.57	4.50	25.3	12.3	9.8	33.0	19.5
Cu-NC-0.5	/	0.51	84.8	8.72	5.92	26.2	15.7	9.4	30.5	18.1

Table S5. Structural parameters of FeCu-NC-0.5 extracted from the Fe K-edge EXAFS fittings

Catalyst	Edge	Path	N[a]	R (Å)[b]	σ^2 (10^{-3}Å^2)[c]	ΔE (eV)[d]	R-factor[e]
FeCu-NC-0.5	Fe	Fe-N	3.8	2.05	1.42	4.08	0.012
		Fe-Fe	2.1	3.73	0.7	-8.32	
	Cu	Cu-N	2.1	1.96	4.9	0.53	0.004
		Cu-O	0.98	1.94	5.5	0.53	

[a]N: coordination numbers; [b]R: bond distance; [c]σ^2: Debye-Waller factors; [d]ΔE: the inner potential correction; [e]R-factor: goodness of fit.

Table S6. Peroxide yields and electron transfer numbers of FeCu-NC-0.5, Fe-NC-0.5, Cu-NC-0.5 and Pt/C catalysts in 0.1 M KOH and 0.05 M PBS electrolytes.

Catalyst	0.1 M KOH		0.05 M PBS	
	Yield of H_2O_2 (%)	*n*	Yield of H_2O_2 (%)	*n*
FeCu-NC-0.5	1.09~4.08	3.91~3.98	1.12~3.70	3.93~3.98
Fe-NC-0.5	0.46~6.62	3.87~3.99	2.22~9.02	3.81~3.95
Cu-NC-0.5	1.61~9.49	3.81~3.97	1.95~9.64	3.81~3.96
Pt/C	2.73~3.78	3.93~3.94	3.59~13.2	3.73~3.93

Table S7. Bader charge analysis for Fe_5-CuN_2O, Fe_5 and CuN_2O models

	Fe_5-CuN_2O		Fe_5	Cu-N_2O
	Fe	Cu	Fe	Cu
Average loss |e|	0.316	0.801	0.313	0.812

Table S8. Gibbs free energy change (ΔG) and overpotential (η) of all computed models at U = 1.23 V followed 4e- path.

Model	ΔG[a] (eV)				η[b] (V)	*d*-band center (eV)
	ΔG_1	ΔG_2	ΔG_3	ΔG_4		
Fe_5-CuN_2O at Fe sites	0.55	-0.78	0.59	-0.37	0.59	-1.28
Fe_5-CuN_2O at Cu sites	0.75	0.34	-1.11	0.02	0.75	/
Fe_5	1.01	-0.73	-0.58	0.31	1.01	-0.92
CuN_2O	0.62	0.03	-0.80	0.17	0.62	/
Fe_5-CuN_4	0.23	0.65	-1.29	0.41	0.65	-1.05
Fe_5-FeN_4	1.03	-0.74	-0.56	0.27	1.03	-0.84

[a] In the ORR process, the *OOH, *O, and *OH are the main reaction intermediates.

The ORR reaction for the four-electron pathway in alkaline solution proceeds according to the following equations:

(1) $O_2(g) + * + H_2O(l) + e^- \rightarrow OOH^* + OH^-$ ΔG_1

(adsorbed O_2 dissociation and protonation into OOH*)

(2) $OOH^* + e^- \rightarrow O^* + OH^-$ ΔG_2 (OOH* decomposition into O*)

(3) $O^* + e^- + H_2O \rightarrow OH^* + OH^-$ ΔG_3 (O* protonation into OH*)

(4) $OH^* + e^- \rightarrow * + OH^-$ ΔG_4 (OH* detachment into OH^-)

Where * is a free adsorption site on the surface.

The ORR reaction for the two-electron pathway in alkaline solution proceeds according to the following equations:

(1) $O_2(g) + * + H_2O(l) + e^- \rightarrow OOH^* + OH^-$ ΔG_1

(Same with that in four-electron pathway at U= 0 V)

(2) $OOH^* + H_2O(l) + e^- \rightarrow H_2O_2 + OH^-$ ΔG_2 ($\Delta G_2 = 1.40 - \Delta G_1$ at U= 0 V)

[b] Overpotential = $\frac{\mathbf{Max}(\Delta G_1, \Delta G_2, \Delta G_3, \Delta G_4)}{e}$

[c] Red data indicated the ΔG for the rate-determining step.

Table S9. Comparison of the ORR performance in 0.1 M KOH and ZAB performance for FeCu-NC-0.5 and dual-atom catalysts previously reported in 6 M KOH electrolyte.

Catalyst	$E_{1/2}$ (V vs RHE)	Metal loading (wt%)		Open-circuit voltage (V)	Power density (mW cm^{-2})	Power density for Pt/C (mW cm^{-2})	Reference
		Fe	Cu				
CuFe10-900	0.889	2.42	2.40	-	200	-	[4]
FC-C@NC	0.85			1.466	118.2	58.3	[5]
FeCu-NC	0.889	1.11	0.36	1.47	91.2	82.8	[6]
FeCu-NC	0.882	2.7	0.74	/	/	/	[7]
Fex/Cu-N@CF	0.944	2.23	0.57	1.4	156	98.7	[8]
20Fe10Cu-NC	0.89	2.42	1.23	/	/	/	[9]
Fe_5-Cu-N-mC	0.92	/	/	1.48	214.8	144.9	[10]
Fe-Cu-N/C	0.89	/	/	/	/	/	[11]
Cu-Fe-N-C	0.864	/	/	/	/	/	[12]
FeCu-NC-0.5	0.883	6.69	1.29	1.53	287.4	207.9	**This work**

Table S10. Comparison of the ORR performance and MFC performance for FeCu-NC-0.5 and non-noble metal catalysts previously reported in 0.05 M PBS electrolyte.

Catalyst	Precursor	Power density (mW m^{-2})	Power density for Pt/C (mW m^{-2})	Reference
FeCu@CN	Cu-MOF	2796	1393	[13]
Fe-Cu-NC-50%	AC[a]	413	/	[14]
AC-N10-900	AC and Melamine	1042		[15]
HD-FeN/G	GO[b] and urea	865	885	[16]
Fe-N/G	CNTs[c] and GO	1210	1080	[17]
Co/Fe-NC	ZIF-67	1831	/	[18]
Fe/N/C-50	Melamine	1166	/	[19]
Cu-NC-T	MOF-199 and melamine	663	815	[20]
Cu-NC-0.5	Melamine and urea	1781	1660	**This work**
Fe-NC-0.5	Melamine and urea	2367	1660	**This work**
FeCu-NC-0.5	Melamine and urea	2578	1660	**This work**

[a] Activated carbon.

[b] Graphene oxide

[c] Carbon nanotube

Reference:

[1] Y. Wang, L. Wu, K. Qu, X. Wang, B. Li, *Carbon*, 228, **2024**, 119429.

[2] X. Wang, Z. He, Y. Shi, B. Li, *J. Electrochem. Soc.*, 164, **2017**, F620.

[3] W. Yang, G. Chata, Y. Zhang, Y. Peng, J.E. Lu, N. Wang, R. Mercado, J. Li, S. Chen, *Nano Energy*, 57, **2019**, 811-819.

[4] H. Yang, T. Zhang, X. Chi, X. Yu, J. Chen, J. Chen, C. Li, S. Tan, Q. He, X. Wang, L. Wang, *J. Mater. Chem. A*, 10, **2022**, 19626-19634.

[5] K. Zhang, Y. Zhang, Q. Zhang, Z. Liang, L. Gu, W. Guo, B. Zhu, S. Guo, R. Zou, *Carbon Energy*, 2, **2020**, 283-293.
[6] M. Xu, L. Zhang, X. Liang, H. Xiao, H. Zhuang, F. Zhang, T. Zhang, P. Han, W. Dai, F. Gao, J. Zhang, L. Zheng, Q. Gao, *Appl. Catal. B-Environ. Energy*, 349, **2024**, 123866.
[7] Z. Xiao, P. Sun, Z. Qiao, K. Qiao, H. Xu, S. Wang, D. Cao, *Chem. Eng. J.*, 446, **2022**, 137112.
[8] S. Wu, S. Jiang, S. Liu, X. Tan, N. Chen, J. Luo, S. Mushrif, K. Cadien, Z. Li, *Energy Environ. Sci.*, 16, **2023**, 3576-3586.
[9] S. Song, X. Zhang, X. Xu, C. Wu, H. Li, Z. Xia, S. Yu, S. Wang, G. Sun, *ChemElectroChem*, 7, **2020**, 3116-3122.
[10] C. Qi, H. Yang, Z. Sun, H. Wang, N. Xu, G. Zhu, L. Wang, W. Jiang, X. Yu, X. Li, Q. Xiao, P. Qiu, W. Luo, *Angew. Chem. Int. Ed. Engl.*, 62, **2023**, e202308344.
[11] W. Fan, Z. Li, C. You, X. Zong, X. Tian, S. Miao, T. Shu, C. Li, S. Liao, *Nano energy*, 37, **2017**, 187-194.
[12] J. Li, J. Chen, H. Wan, J. Xiao, Y. Tang, M. Liu, H. Wang, *Appl. Catal. B-Environ.*, 242, **2019**, 209-217.
[13] H. Li, H. Shi, Y. Dai, H. You, S.R.B. Arulmani, H. Zhang, C. Feng, L. Huang, T. Zeng, J. Yan, *J. Colloid Interf. Sci.*, 628, **2022**, 652-662.
[14] L. Ren, J. Lu, H. Liu, *New J. Chem.*, 46, **2022**, 21579-21590.
[15] X. Tian, M. Zhou, M. Li, C. Tan, L. Liang, P. Su, *Fuel*, 223, **2018**, 422-430.
[16] Y. Liu, X. Jin, D. Dionysiou, H. Liu, Y. Huang, *J. Power Sources*, 278, **2015**, 773-781.
[17] D. Wang, Z. Ma, M. Zhang, N. Zhao, H. Song, *RSC advances*, 8, **2018**, 1203-1209.
[18] B. Liang, M. Su, Z. Zhao, S. Liang, *J. Electroanal. Chem.*, 962, **2024**, 118260.
[19] D. Wang, J. Hu, J. Yang, K. Xiao, S. Liang, J. Xu, B. Liu, H. Hou, *Int. J. Hydrogen Energy*, 45, **2020**, 3163-3175.
[20] C. Su, W. Wang, B. Jiang, M. Zhang, Y. Wang, H. Wang, H. Song, *Electroanalysis*, 35, **2023**, e202200266.